J Sci Comput
DOI 10.1007/s10915-010-9444-4

# Hydrodynamic Instabilities in Well-Balanced Finite Volume Schemes for Frictional Shallow Water Equations. The Kinematic Wave Case

**Patricio Bohorquez · Martin Rentschler**

Received: 15 December 2009 / Revised: 22 July 2010 / Accepted: 29 November 2010


**Abstract** We report the developments of hydrodynamic instabilities in several well-balanced finite volume schemes that are observed during the computation of the temporal evolution of an out-balance flow which is essentially a kinematic wave. The numerical simulations are based on the one-dimensional shallow-water equations for a uniformly sloping bed with hydraulic resistance. Subsequently, we highlight the need of low dissipative high-order well-balanced filter schemes for non-equilibrium flows with variable cut-off wavenumber to compute the out-balance flow under consideration, i.e. the kinematic wave.

**Keywords** One layer shallow water · Kinematic wave · Roll waves · WENO schemes · Compact filter

## 1 Introduction

This paper is aimed at reporting the growth of hydrodynamic instabilities in several well-balanced finite volume schemes that is observed during the computation of the temporal evolution of an out-balance flow which is essentially a kinematic wave [1]. The numerical simulations will be based on the one-dimensional shallow-water equations for uniformly sloping beds with hydraulic resistance. Though observed instabilities are of numerical origin, we shall stress the point that in the end they correspond to genuine solutions of the exact system of hyperbolic balance laws with source terms, referred hereafter to as roll waves [2].

In the shallow-water approximation, the dimensionless equations for the mass conservation and momentum in the direction of the flow over a constant slope bed sketched in Fig. 1

P. Bohorquez (✉)
Área de Mecánica de Fluidos, Departamento de Ingeniería Mecánica y Minera, Universidad de Jaén, Campus de las Lagunillas, 23071 Jaén, Spain
e-mail: patricio.bohorquez@ujaen.es

M. Rentschler
School of Architecture, Civil and Environmental Engineering, École Polytechnique Fédérale de Lausanne, 1015 Lausanne, Switzerland
e-mail: martin.rentschler@epfl.ch

Published online: 08 December 2010

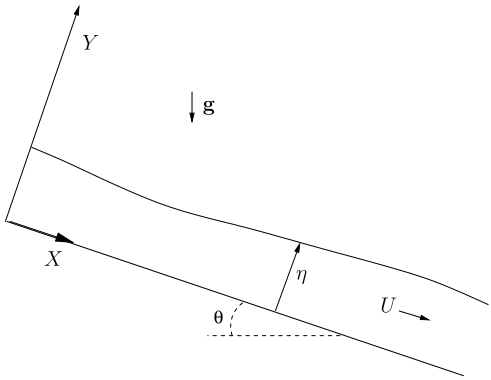


**Fig. 1** Coordinates and sketch of the flow on an inclined plane, illustrating the sloping flow configuration for $0 < \theta < \pi/2$

can be written as [3]

$$\frac{\partial \boldsymbol{\omega}}{\partial t} + \frac{\partial \mathbf{F}(\boldsymbol{\omega})}{\partial X} = \mathbf{S}(\boldsymbol{\omega}), \quad X \geq 0,\ t > 0, \tag{1}$$

in which

$$\begin{aligned} \boldsymbol{\omega}(X,t) &= \begin{pmatrix} \eta \\ Q \end{pmatrix}, \qquad \mathbf{F}(\boldsymbol{\omega}) = \begin{pmatrix} Q \\ \frac{Q^2}{\eta} + \cos\theta \frac{\eta^2}{2} \end{pmatrix}, \\ \mathbf{S}(\boldsymbol{\omega}) &= \begin{pmatrix} 0 \\ \eta \sin\theta - \frac{f Q^2}{8\eta^2} \end{pmatrix}, \end{aligned} \tag{2}$$

where $\theta$ is the angle between the bed and the horizontal, $0 < \theta < \pi/2$; $t$ is time; $X$ is the coordinate along the bed; $\eta$ is the depth of the water measured along the coordinate $Y$ perpendicular to the bed; $Q$ is the flow rate per unit width; $U \equiv Q/\eta$ is the depth-averaged velocity component along $X$; and $f$ is the Darcy-Weisbach friction factor (assumed constant in order to make the analytical treatment feasible). All the variables in these equations have been non-dimensionalized with respect to a length scale $\eta_0$, corresponding to some initial depth, and a velocity scale $U_0 \equiv \sqrt{g\eta_0}$, where $g$ is the acceleration because of gravity.

We focus our attention on out-equilibrium shallow-water flows in which the shallowness parameter ($\epsilon \equiv \eta_0/l$ with $l$ being the scaled characteristic streamwise extent occupied by the flow) vanishes as time infinity, i.e. $\epsilon \to 0$ as $t \to \infty$. In that scenario, the non-dimensional variables $X$ and $t$ are not suited to describing the evolution of the ensuing flow, which varies on a much slower scale:

$$\hat{x} = \epsilon X, \qquad \hat{t} = \epsilon t \quad \text{with } \epsilon \equiv \frac{\eta_0}{l} \ll \tan\theta. \tag{3}$$

In these new variables, (1) reads

$$\frac{\partial \boldsymbol{\omega}}{\partial \hat{t}} + \frac{\partial \mathbf{F}(\boldsymbol{\omega})}{\partial \hat{x}} = \epsilon^{-1} \mathbf{S}(\boldsymbol{\omega}), \quad \hat{x} \geq 0,\ \hat{t} > 0. \tag{4}$$

At leading order we obtain $\mathbf{S}(\boldsymbol{\omega}) = 0$ as $\epsilon$ vanishes, and we get a state whereby the friction of the fluid balances everywhere the gravitational pull down the incline. The resulting flow is known as 'kinematic wave' [1]. The system of hyperbolic balance laws (4) admits regular solutions of the form $\boldsymbol{\omega} = \sum_{i=0} \epsilon^i \boldsymbol{\omega}_i$ [3]. The leading-order term of the regular solution,

$\boldsymbol{\omega}_0 \equiv (H_0, H_0 V_0)^T$, where superscript $T$ denotes the transposed vector, satisfies the well-known kinematic wave equation,

$$H_0 = \frac{f V_0^2}{8 \sin\theta}, \qquad \frac{\partial V_0}{\partial \hat{t}} + \frac{3 V_0}{2} \frac{\partial V_0}{\partial \hat{x}} = 0, \quad \hat{x} \geq 0, \ \hat{t} > 0, \tag{5}$$

showing that $H_0$ and $V_0$ remain constant on characteristics propagating with velocity $(3/2)V_0$, referred to as 'expansion fan'. Furthermore, higher-order corrections vanish as time infinity [3, Appendix A] and (5) does not have steady-state solution for $V_0(\hat{x}, 0) \neq 0$. It is worth recalling that the source terms in (4) dominate the dynamics in such scenario and that $\partial \boldsymbol{\omega} / \partial \hat{t} \ll \mathbf{S}(\boldsymbol{\omega})$. Therefore, the adoption of well-balanced numerical methods (which are able to resolve quasi-steady problems) become an interesting option. In the case of shallow water flows with moving water, different well-balanced methods have been developed [4, 5], and specific formulations have been presented for hyperbolic system of balance laws in the presence of stiff source terms [6] as well as multiscale phenomena [7]. However, in the present work we shall restrict our analysis to well-balanced schemes in the sense described in [8, 9].

One of us [3] has presented a linear stability analysis of (1) by means of a multiple-scale analysis in space and time for the flow whose initial conditions ($t = 0$) are

$$U(X, 0) = V_0(X, 0) = \vartheta X, \qquad \eta(X, 0) = H_0(X, 0) = \frac{f V_0^2}{8 \sin\theta}, \quad X \geq 0, \tag{6}$$

with $0 < \vartheta \ll 1$, showing that there exists a critical Froude number $Fr_{cr}$ above which the background flow becomes unstable. The ensuing background flow is essentially a kinematic wave, and its local Froude number is given by

$$Fr_p \equiv \frac{V_0}{\sqrt{H_0 \cos\theta}} = \sqrt{\frac{8}{f} \tan\theta}. \tag{7}$$

The critical Froude number $Fr_{cr}(\phi)$,

$$Fr_{cr}(\phi) \equiv \left[ \frac{8\phi^2}{1 + 4\phi + 2\phi^2 - (1+\phi)\sqrt{1 + 6\phi + 3\phi^2}} \right]^{1/2}, \tag{8}$$

which depends on the local slope of the free-surface height $\phi$,

$$\phi \equiv \frac{V_0}{\sin\theta} \frac{\partial V_0}{\partial X}, \tag{9}$$

is always larger than 2 for $\phi > 0$ and tends to the critical value of the plane-parallel flow of 2 [10] as $\phi \to 0$ (see Fig. 2(a)). In addition, for $Fr_p > Fr_{cr}$, we have reported the existence of a cutoff wavelength $\lambda_\infty$ for the unstable spectrum: the kinematic wave is stable at all wavelengths $\lambda$ within the range $\lambda_\infty \leq \lambda < \infty$,

$$\lambda_\infty \equiv \frac{2\pi V_0^2}{\sin\theta} \sqrt{\frac{2 + \phi}{32\phi(1+\phi)^2}}. \tag{10}$$

Figure 2(b) illustrates the dependence of $\lambda_\infty$ with $\phi$. We refer the reader to [3] for further details on the stability analysis.

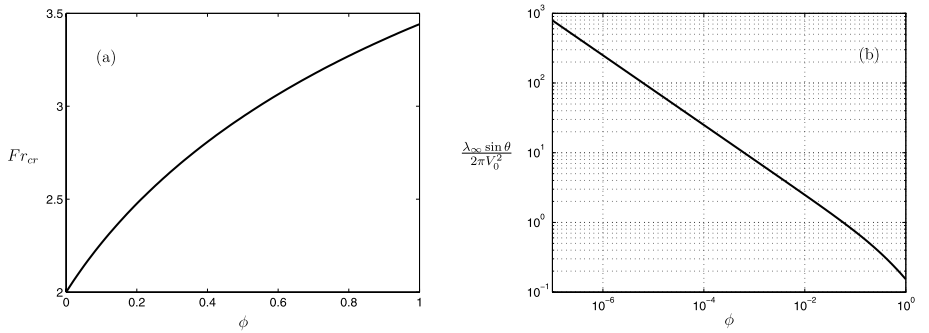


**Fig. 2** $Fr_{cr}$ (**a**) and $\lambda_\infty$ (**b**) as functions of $\phi > 0$

We start with the formulation of the problem, the definition of some asymptotic solutions and the description of the numerical schemes (Sect. 2). Subsequently, in Sect. 3, we compute numerically both the base flow and the decay of infinitesimal disturbances superimposed about a kinematic wave and present some cases that exhibit the spontaneous formation of physical instabilities. The latter result will be justified in view of the unstable nature of the kinematic wave. Finally, we draw some conclusions.

## 2 Formulation of the Problem

Here we shall analyze the accuracy of several finite volume schemes to compute the evolution of infinitesimal disturbances which are superimposed on a kinematic wave. To that end, if $\eta = H_0(X,t)$ and $U = V_0(X,t)$ is a solution to the equations, the perturbed flow is decomposed, as usual, as the sum of the basic flow solution, $H_0$ and $V_0$, plus a small perturbation, $\upsilon h(X,t)$ and $\upsilon u(X,t)$, i.e. $(\eta, U)^T = (H_0, V_0)^T + \upsilon(h,u)^T$ with $\upsilon \ll 1$. In particular, we solve (1)–(2) for a perturbed kinematic wave whose initial condition ($t = 0$) is

$$\begin{bmatrix} \eta(X,0) \\ U(X,0) \end{bmatrix} = \begin{bmatrix} H_0(X,0) \\ V_0(X,0) \end{bmatrix} + \upsilon \begin{bmatrix} h(X,0) \\ u(X,0) \end{bmatrix}, \quad 0 < X_{b0} \le X \le X_{b3}, \tag{11}$$

in which $H_0(X,0)$ and $V_0(X,0)$ are given by (6). In order to compare the numerical results with previous known asymptotic solutions for the evolution of small disturbances (see below), we shall restrict our attention to the initial conditions for $(h,u)^T$ analyzed in [3, Sect. 3.1],

$$\begin{bmatrix} h(X,0) \\ u(X,0) \end{bmatrix} = F \begin{bmatrix} \frac{f\vartheta X}{4\sin\theta} \\ 1 \end{bmatrix} + \upsilon F \begin{bmatrix} \frac{1}{4\cos\theta}(F + 2XF') \\ \frac{1}{\vartheta}F' \end{bmatrix} + \upsilon^2 \frac{F}{4\vartheta} \begin{bmatrix} \frac{1}{\cos\theta}[2X(F')^2 + F(2F' + XF'')] \\ \frac{2}{\vartheta}[2(F')^2 + FF'] \end{bmatrix}, \tag{12}$$

where $F \equiv F(X)$ and the prime denotes the differential operator with respect to $X$. For the sake of simplicity, in the present work we analyze the response to sinusoidal disturbances,

$$F(X) = \begin{cases} \sin\left[\frac{2\pi}{\lambda_0}(X - X_{b1})\right] & \text{if } X_{b1} \le X \le X_{b2}, \\ 0 & \text{otherwise,} \end{cases} \qquad X_{b0} < X_{b1},\ X_{b2} < X_{b3}, \tag{13}$$

where $\lambda_0$ is the initial wavelength of the disturbance; $X_{b2} = X_{b1} + n\lambda_0$; and $n$ represents the number of waves introduced as perturbations.

Taking into account that we shall analyze base flows with $Fr_p \geq 2$, we conclude that the flow is supercritical and, thus, two physical boundary conditions (BCs) are to be imposed at the inlet and no physical outflow BCs are to be applied. Inflow BCs are obtained by evaluating (14) at the inflow ghostcells required by the numerical scheme (see below),

$$V_0(X,t) = \vartheta\xi(X,t), \qquad H_0(X,t) = \frac{fV_0^2}{8\sin\theta}, \qquad h(X,t) = u(X,t) = 0, \quad 0 \leq t. \tag{14}$$

For notational clarity, we have introduced the new variables $\xi(X,t)$ and $\tau(t)$:

$$\xi(X,t) \equiv \frac{2X}{2+3\vartheta t}, \qquad \tau(t) \equiv 1 + \frac{3}{2}\vartheta t. \tag{15}$$

In the particular case $Fr_p = 2$, where the plane-parallel Froude number $Fr_p$ is defined by (7), the exact solution to (1)–(2) for the initial and boundary conditions given by (11) and (14), respectively, can be written as functions of $\{\xi, \tau\}$ [3]:

$$\begin{bmatrix} \eta(\xi,\tau) \\ U(\xi,\tau) \end{bmatrix} = \begin{bmatrix} \frac{f(\vartheta\xi)^2}{8\sin\theta} \\ \vartheta\xi \end{bmatrix} + \upsilon\frac{F}{\tau}\begin{bmatrix} \frac{f\vartheta\xi}{4\sin\theta} \\ 1 \end{bmatrix} + \upsilon^2\frac{F}{\tau^2}\begin{bmatrix} \frac{1}{4\cos\theta}(F+2\xi F') \\ \frac{1}{\vartheta}F' \end{bmatrix} + \upsilon^3\frac{F}{4\vartheta\tau^3}\begin{bmatrix} \frac{1}{\cos\theta}[2\xi(F')^2 + F(2F'+\xi F'')] \\ \frac{2}{\vartheta}[2(F')^2 + FF'] \end{bmatrix}, \tag{16}$$

with some abuse of notation, we have also noted by $F$ the function $F(\xi)$. This solution may serve to validate numerical codes that solve the full shallow-water equations (1)–(2). Hence, (16) is used in the next section to check the capabilities of several well-balanced finite volume schemes to compute the amplitude, wavelength and phase speed of small non-linear perturbations.

Furthermore, (16) is not only an exact solution to (1)–(2) for $Fr_p = 2$ but also an asymptotic solution for $Fr_p > 2$ when $\phi \ll 1$—typically $\phi$ (9) should be $O(10^{-4})$ to avoid non-normal effects—and $\lambda_0 > \lambda_\infty(\phi, V_0, \theta)$ (10) at $t = 0$ [3]. Notice that, according to (16), the normalized perturbation $(h,u)^T$ decays and its wavelength increases linearly with time at a rate independent of the initial wavelength $\lambda_0$ and of the plane-parallel Froude number $Fr_p$ (7). Conversely, for $\lambda_0 < \lambda_\infty$ and values of $Fr_p$ (7) greater than $Fr_{cr}$ (8), the normalized perturbation $(h,u)^T$ will grow ultimately developing hydraulic jumps. In the present work we focus the attention just on the former case.

Finally, the initial set-up for the unperturbed (background) flow is obviously exactly the same as for the perturbed flow but setting $\upsilon = 0$ in (11). Figure 3(a) illustrates the typical ensuing velocity profile $V_0(X,t)$ of the kinematic wave at several instants of time, which is obtained by setting $\upsilon = 0$ in (16). Notice that $V_0(X,t)$ is independent of the plane-parallel Froude number $Fr_p$. Apparently, the problem at hand is fairly simple. For completeness, Fig. 3(b) shows the temporal evolution of a stable wave packet formed by three infinitesimal disturbances ($n = 3$). Similar to Fig. 3(a), we plot the disturbance velocity $\upsilon u(X,t)$, which is obtained by subtracting $V_0(X,t)$ from (16). As stated above, the perturbation decays and its wavelength increases as time proceeds.

The asymptotic results are employed here to quantify the accuracy of several finite volume methods to compute both the base flow $[H_0(X,t), V_0(X,t)]^T$ and the decay of infinitesimal perturbations $\upsilon[h(X,t), u(X,t)]^T$. To that end, the non-linear set of (1)–(2) is solved

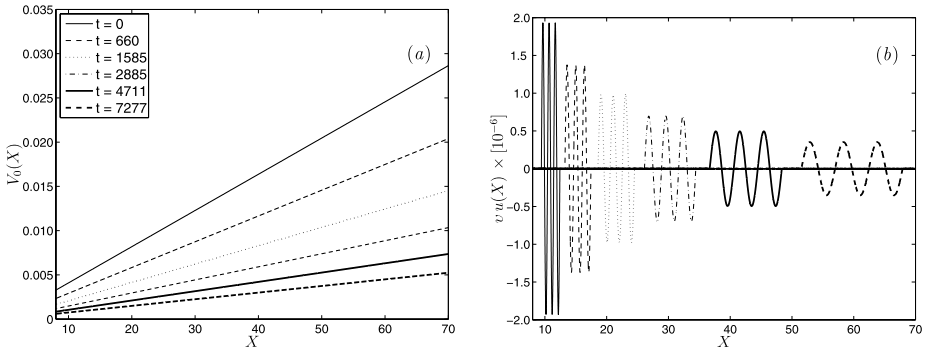


**Fig. 3** (**a**) Kinematic wave velocity profile $V_0(X,t)$ and (**b**) perturbation velocity $\upsilon u(X,t)$ at several instants of time $t$ for $\vartheta \approx 4.1 \times 10^{-4}$, $X_{b0} = 6.425$, $X_{b1} = 9.425$, $X_{b2} = 12.425$, $X_{b3} = 70$, $\upsilon \approx 2 \times 10^{-6}$, $\lambda_0 = 1$, $\theta = 1^\circ$

in the computational domain with cells $\mathcal{C}_i = (X_{i-1/2}, X_{i+1/2})$, $i = 1, \ldots, Nx$, for the initial and boundary conditions given by (11) and (14), respectively. The computational variables are $\mathbf{Q}_i^n$, which approximate the average value over the $i$th interval at time $t_n$:

$$\mathbf{Q}_i^n \equiv \begin{pmatrix} \overline{\eta}_i^n \\ \overline{\eta U}_i^n \end{pmatrix} \approx \frac{1}{\Delta X_i} \int_{\mathcal{C}_i} \begin{pmatrix} \eta \\ \eta U \end{pmatrix} (X, t_n) dX, \quad \Delta X_i = X_{i+\frac{1}{2}} - X_{i-\frac{1}{2}}, \tag{17}$$

where the centre of the cell is $X_i = (X_{i+1/2} + X_{i-1/2})/2$. For simplicity we assume a uniform grid with cell size $\Delta X_i = \Delta X$. We use three different finite volume schemes, namely that: first-order upwind and second-order TVD-Minmod numerical scheme with semi-implicit and upwind treatment of the source term [8] (denoted by UPW1 and TVD2, respectively); fifth-order accurate, weighted essentially nonoscillatory (WENO) scheme with second-order accurate, source term upwinding [9] and third-order accurate, strong stability-preserving (SSP), Runge-Kutta time integration [11] (denoted by WENO2). Characteristic-wise reconstruction is employed in WENO2 in order to compare with previous known results for componentwise reconstruction [3]. Left- and right-going flux differences are computed using Roe's approximate Riemann solver with entropy fix for transonic rarefactions. Both reconstruction schemes, as well as the wave-slope and transmission-based reconstruction, are implemented by default in SharpClaw, the new incarnation of WENOCLAW [12] which has been adapted here to perform the WENO2 simulations in Sect. 3. In doing so, our WENO2 implementation is equivalent to the original scheme proposed in [9, Sects. 2 & 4.1]. Inflow BCs are obtained by evaluating (14) at $X = X_{1/2}$, $X = X_{-1/2}, X_{1/2}$ and $X = X_{-3/2}, X_{-1/2}, X_{1/2}$ for first-, second- and fifth-order accuracy in space, respectively. Finally, outflow boundary conditions have been undertaken using the characteristic variable extrapolation (CVE) method.

## 3 Results

For $Fr_p = 2$, Fig. 4(a) shows the comparison between the exact solution for the amplitude of the velocity perturbation and the numerical results obtained with the finite volume methods described in the previous section. As expected, the upwind method badly smears the disturbance and introduces excessive dissipation in the numerical solution overpredicting the

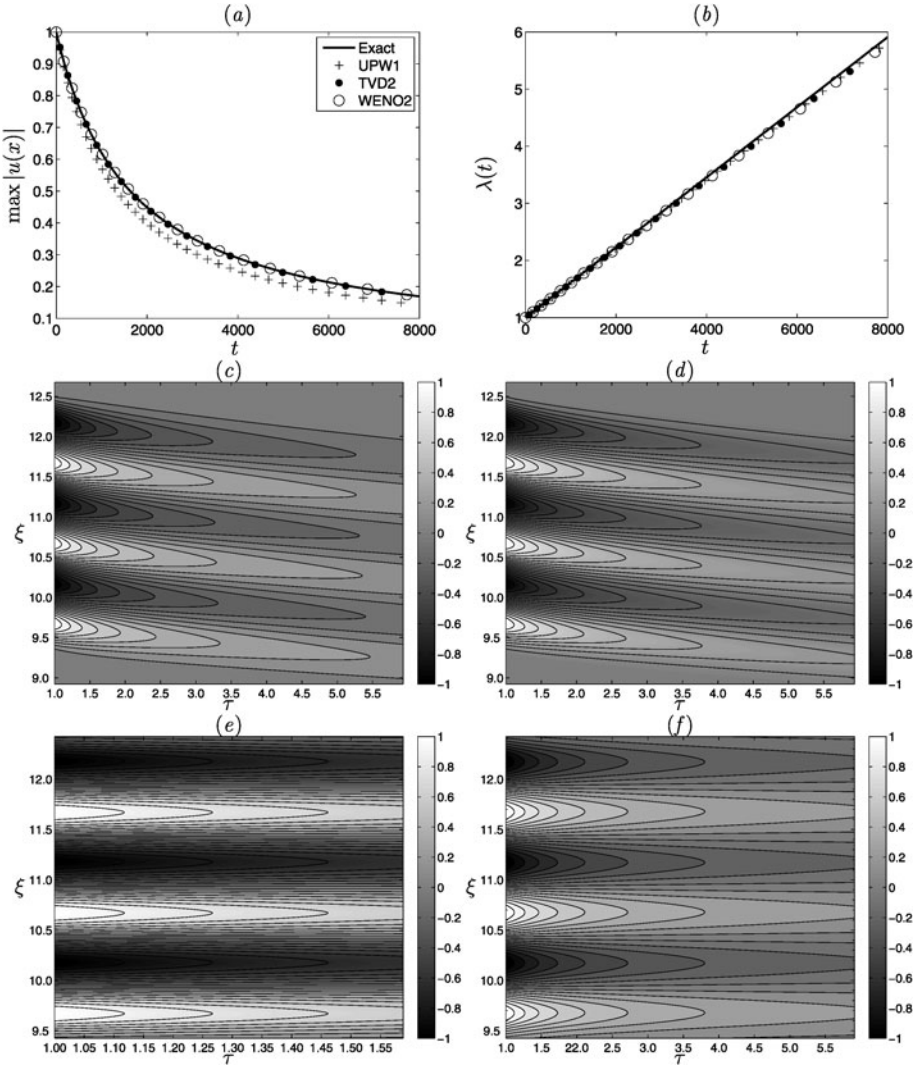


**Fig. 4** Comparison between the non-linear numerical and the analytical solutions of the disturbance velocity: (**a**) amplitude, normalized with respect to $\upsilon$, and (**b**) wavelength as function of time $t$ for the numerical simulations depicted in subplots (**c**)–(**d**) and (**f**). Isocontours of non-linear numerical perturbations in the $\{\tau, \xi\}$-plane for (**c**) UPW1 with a Courant-Friedrichs-Lewy (CFL) number of CFL $= 0.4$, (**d**) TVD2 with CFL $= 0.4$, (**e**) TVD2 with CFL $= 0.01$, and (**f**) WENO2 with CFL $= 0.4$. The numerical experiment is defined by the same values as for Fig. 3. The computations were conducted with $\Delta X = 10^{-3}$, corresponding to 1000 nodes per disturbance at $t = 0$

decay rate. The TVD method is much less dissipative and sharpens up the overly diffusive upwind approximation. Higher-order methods, such as the WENO, give more antidiffusive solutions and better predict the exact solution. The three numerical techniques are able to compute with accuracy the numerical wavelength, see Fig. 4(b), which has been determined by considering the distance between consecutive corresponding points of the same phase, such as crests. Subsequently, in order to analyze the errors arising from the numerical group

**Table 1** $L^1$ errors and numerical orders of accuracy for the example in Fig. 5(a) with $6.425 < X < 7.425$ and $t = 500$ ($\tau \approx 1.31$)

| $\Delta X$ | CFL | $\eta$ | | $U$ | |
|---|---|---|---|---|---|
| | | $L^1$ error | Order | $L^1$ error | Order |
| 4.00E-03 | 0.5 | 2.14E-08 | | 2.24E-08 | |
| 2.00E-03 | 0.5 | 5.34E-09 | 2.00 | 5.16E-09 | 2.11 |
| 1.00E-03 | 0.5 | 1.33E-09 | 2.00 | 1.21E-09 | 2.10 |
| 5.00E-04 | 0.5 | 3.33E-10 | 2.00 | 2.94E-10 | 2.03 |
| 2.50E-04 | 0.5 | 8.34E-11 | 2.00 | 7.31E-11 | 2.01 |
| 1.25E-04 | 0.5 | 2.11E-11 | 2.11 | 1.81E-11 | 1.98 |

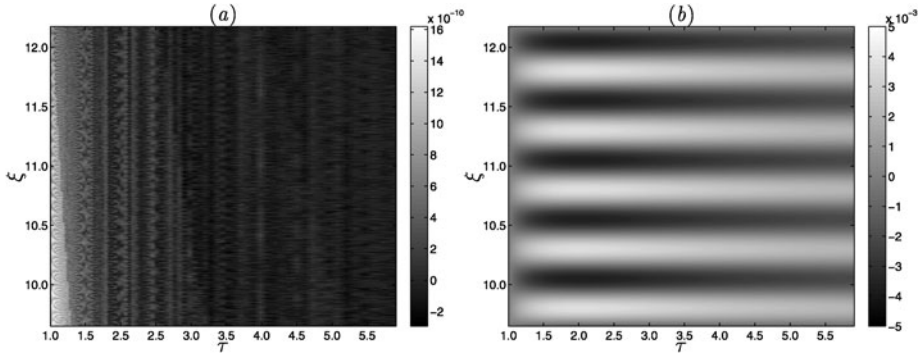


**Fig. 5** Quantification of the errors in the numerical simulation shown in Fig. 4(d) for (**a**) the background flow $V_0(\xi, \tau)$, i.e. for the kinematic wave, and (**b**) for the normalized disturbance velocity $u(\xi, \tau)$. The errors are defined as (**a**) $(V_0 - \overline{V}_0)/V_0$ and (**b**) $u - \overline{u}$, where the overline denotes the numerical solution

velocity of the method, we have represented the numerical solution of the disturbances in a moving reference frame propagating on the expansion fan. Both the upwind and TVD methods propagate the disturbances at an incorrect speed, as shown in Figs. 4(c)–(d), though this error can be eliminated by decreasing the time step (see Fig. 4(e)). On the other hand, WENO propagates the disturbances at the correct speed on trajectories which are given by constant values of $\xi$ in the $\{\tau, \xi\}$-plane, as illustrated in Fig. 4(f).

The accuracy of the WENO numerical solution is quantified in Fig. 5. In order to measure the relative errors in the base flow computation, we have performed a numerical experiment in the same conditions as for Fig. 4 but setting $\upsilon = 0$ in (11). Next, the numerical results have been compared with the exact solution $V_0(X, t)$ given by (14), which equals (16) with $\upsilon = 0$. Figure 5(a) shows that the relative errors lie below $10^{-9}$. Additionally, Table 1 contains the grid-function norm of the relative errors for the cell averages and the numerical orders of accuracy for the WENO scheme. Subsequently, the error in the disturbance computation is readily obtained by subtracting the exact solution $U$, given by (16), from the numerical result shown in Fig. 4(f). By normalizing the absolute error with respect to $\upsilon$, see Fig. 5(b), we find that the relative errors are $O(10^{-3})$. The actual numerical errors are of the same order of magnitude than those previously reported by using componentwise reconstruction [3] instead of characteristic-based reconstruction, and so we conclude that the present computations are extremely well resolved with 1000 cells per perturbation wavelength, whilst differences may arise when coarser resolutions are used.

Before presenting numerical results for a scenario where the local Froude number $Fr_p$ (7) is increased above the critical value $Fr_{cr}$ (8), whilst the remaining parameters take the

**Table 2** Each cell lists the growth rate $\hat{\gamma} \equiv \mathrm{Re}(2\hat{\lambda})$, with $\hat{\lambda}$ given by (19), for $V_0 = 0.0145$, $\theta = 1^\circ$, $\phi = 10^{-4}$, $\lambda = \{0, 10^{-3}, 10^{-2}, 10^{-1}, 1, 10, 10^2\}$ and $Fr_p$={2, 2.1, 3, 4, 5, 10}

| $\lambda$ | $Fr_p = 2$ | $Fr_p = 2.1$ | $Fr_p = 3$ | $Fr_p = 4$ | $Fr_p = 5$ | $Fr_p = 10$ |
|---|---|---|---|---|---|---|
| 0 | −7.22E-04 | 2.40E-01 | 2.41E+00 | 4.81E+00 | 7.22E+00 | 1.93E+01 |
| 1E-03 | −7.22E-04 | 2.40E-01 | 2.40E+00 | 4.77E+00 | 7.09E+00 | 1.62E+01 |
| 1E-02 | −7.38E-04 | 2.22E-01 | 1.92E+00 | 3.11E+00 | 3.79E+00 | 4.82E+00 |
| 1E-01 | −9.32E-04 | 2.71E-02 | 1.65E-01 | 2.23E-01 | 2.50E-01 | 2.84E-01 |
| 1E+00 | −9.63E-04 | −6.42E-04 | 9.50E-04 | 1.62E-03 | 1.93E-03 | 2.34E-03 |
| 1E+01 | −9.63E-04 | −9.60E-04 | −9.44E-04 | −9.37E-04 | −9.34E-04 | −9.30E-04 |
| 1E+02 | −9.63E-04 | −9.63E-04 | −9.63E-04 | −9.63E-04 | −9.63E-04 | −9.63E-04 |

same values as for Fig. 4, it is convenient to introduce the scaled, complex wavenumber $a$,

$$a \equiv i \frac{2\pi V_0^2}{\lambda \sin\theta}. \tag{18}$$

From [3, Sect. 3.2.1], the least stable eigenvalue $\hat{\lambda}$ of the near-parallel, linear perturbation equations associated with $a$ is

$$\hat{\lambda} = -\frac{\sin\theta}{V_0}\Big\{2(1+a+\phi) - \sqrt{2}\sqrt{2+2a^2\varrho-4\phi+(8\varrho-2)\phi^2+a[(8\varrho-1)\phi-2]}\Big\}, \tag{19}$$

where $\varrho \equiv Fr_p^{-2}$, and so the physical growth rate is computed as $\hat{\gamma} \equiv \mathrm{Re}(2\hat{\lambda})$. Table 2 indicates that, for a fixed value of $V_0 = 0.0145$, $\theta = 1^\circ$ and $\phi = 10^{-4}$, the physical growth rate $\hat{\gamma}$ monotonously increases (decreases) with both the wavenumber (wavelength) and the plane-parallel Froude number $Fr_p$ for $Fr_p > Fr_{cr} \approx 2.0003$. Notice that $\hat{\gamma}$ is negative at all wavelengths for $Fr_p < Fr_{cr}$, i.e. the background flow is locally stable. For $Fr_p =$ constant, it is an easy exercise to show that $\hat{\gamma}$ reaches the maximum value as $\lambda \to 0$,

$$\hat{\gamma}_{max} \equiv \lim_{\lambda\to 0}\hat{\gamma} = \frac{2\sin\theta}{V_0}\left(-2-2\phi+\frac{2+\phi-8\rho\phi}{2\sqrt{\rho}}\right), \tag{20}$$

as shown in the first row of Table 2.

Since the growth rate monotonously increases with the wavenumber, and taking into account that it is positive for $Fr_p > Fr_{cr}$ and $\lambda \to 0$, the problem becomes ill-posedness when $Fr_p > Fr_{cr}$. Indeed, Fig. 6(a) shows the developments of the unstable waves by increasing the plane-parallel Froude number $Fr_p$ up to 4 whilst the remaining parameters take the same values as for Fig. 4. We observe the growth of free-surface instability waves with wavelengths of, approximately, $8\Delta X$, see the inset (i) of Fig. 6(a), which coarse and ultimately grow to reach the stage at which the velocity profile has the aspect of the classical roll waves [2], as shown in the inset (ii). The evolution of the surface is therefore governed by the same sequence of transitions which are observed in experiments [e.g. 2]: starting from the primary instability of the plane-parallel flow, filtering mechanism of the linear instability and secondary modulation instability that converts the primary wave field into a roll wave. In order to identify the most unstable mode growing, Figs. 6(b)–(c) show additional results for

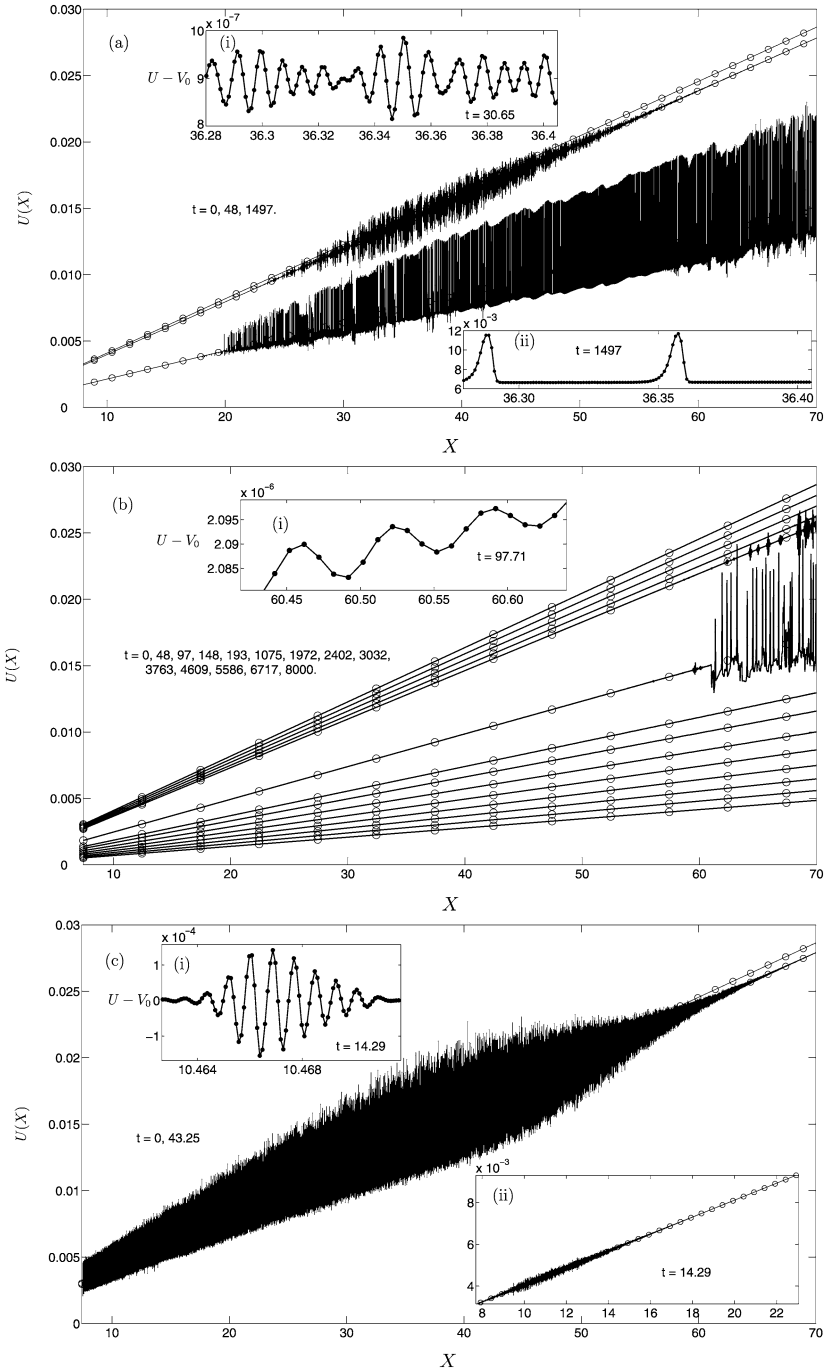


**Fig. 6** Onset of hydrodynamic instabilities in the same conditions as for Fig. 4(f) but increasing the Froude number up to $Fr_p = 4$: (**a**) $\Delta X = 10^{-3}$, (**b**) $\Delta X = 10^{-2}$, (**c**) $\Delta X = 10^{-4}$. The asymptotic solution (14) is shown in *open circles*, whilst the numerical simulation is shown in *continuous line* (*solid dots* depict grid points)

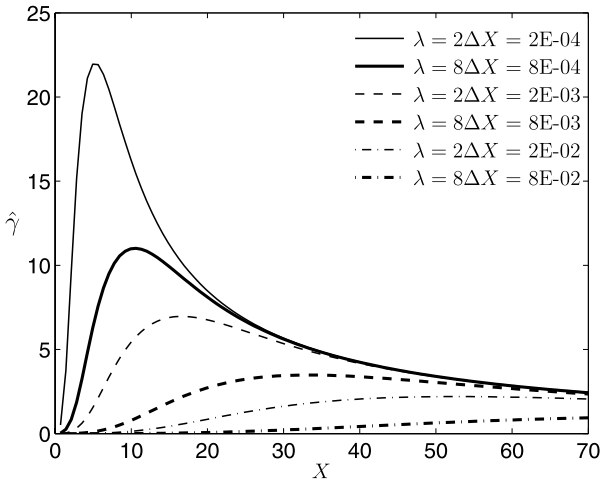


**Fig. 7** Local growth rate $\hat{\gamma}$ at $t = 0$ for the same conditions as for Fig. 6, $\lambda = \{2\Delta X, 8\Delta X\}$ and $\Delta X = \{10^{-4}, 10^{-3}, 10^{-2}\}$

a coarser and a finer mesh, respectively. On the one hand, inset (i) of Figs. 6(a)–(c) clearly illustrates that the wavelengths of the oscillations at onset are, approximately, of $8\Delta X$. On the other hand, the mesh size $\Delta X$ fixes the location where unstable disturbances with $\lambda = 8\Delta X$ start to grow: for $\Delta X = 10^{-3}$, unstable waves develop in the middle of the computational domain, see the numerical solution at $t = 48$ in Fig. 6(a), which are convected downstream because of the convective nature of the instabilities [3]; when increasing the mesh size up to $\Delta X = 10^{-2}$, the inception occurs further downstream (i.e. $X > 60$) at $t \approx 97$, and the disturbances reach a nonlinear saturated solution at $t \approx 1075$, which is later attenuated ($t \geq 1972$); finally, for a finer mesh with $\Delta X = 10^{-4}$, instabilities develop further upstream and close to the inlet, as shown in inset (ii) of Fig. 6(c). Such behavior is physically correct because numerical instabilities grow where the physical growth rates reach their maximum values, see Fig. 7: $X \approx 10$ for $\Delta X = 10^{-4}$, $X \approx 30$ for $\Delta X = 10^{-3}$ and $X > 60$ for $\Delta X = 10^{-2}$. However, though disturbances with $\lambda = 2\Delta X$ are more unstable than those with $\lambda = 8\Delta X$, we did not find their developments by visual inspection, at least with amplitudes relative to the base flow larger than $10^{-4}\%$. But these very high wavenumbers are too extreme to be physically meaningful.

In view of the present results, we conclude that the numerical solutions reflect the physical situation properly and the ultimate nonlinear saturated solutions may well have good physical meaning. As a matter of fact, roll-waves were observed in the final stage of a water dam-break flood at the US Geological Survey debris-flow flume, where hydrodynamic instabilities developed at late time when the bulk of the flood wave reached a quasi-uniform and quasi-steady state [3]. Furthermore, it is worth mentioning that our numerical simulations do not blow up and, even more, they recover the stable state at late time when the disturbances are attenuated until their ultimate extinction (e.g., see Fig. 6(b)).

The above-described phenomenon has been observed not only by using the characteristic-based reconstruction but also for the componentwise, wave-slope and transmission-based reconstruction [12]. For this reason, the comparison between the asymptotic (16) and the numerical solution for the attenuation of the infinitesimal disturbances $(h, u)^T$ can only be done in the region that is not affected by hydrodynamic instabilities, which is approximately $X < 20$ in the numerical simulation shown in Fig. 6 (a). The supporting comparison has been reported in [3] and is omitted here for the sake of the brevity. Moreover, even the second-order TVD numerical scheme exhibits the development of surges after a few time steps,

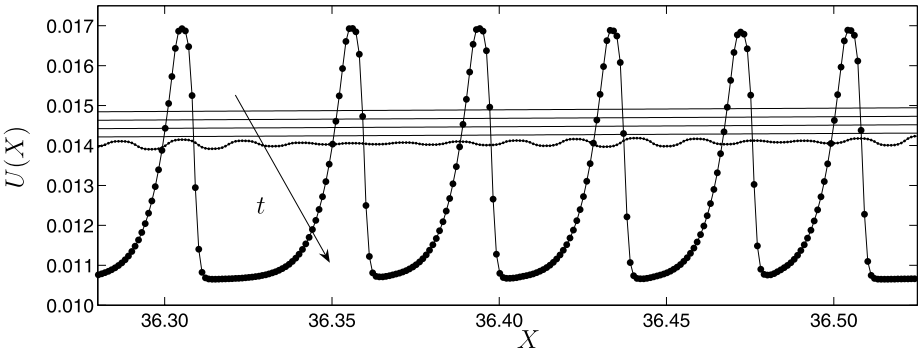


**Fig. 8** Onset of hydrodynamic instabilities in the same conditions as for Fig. 4(d) but increasing the Froude number up to $Fr_p = 4$: $t = 0, 24, 48, 72, 97, 371$

see Fig. 8. The authors have also verified the same phenomenon for the first-order upwind scheme, though the development of free-surface instabilities is delayed because of the overly diffusive upwind approximation. Finally, by simulating numerically the same configuration but setting $\upsilon = 0$, we have found analogous results.

It is worth noting that in the case of a steady, uniform flow over a constant slope bed all the numerical schemes have computed with success the analytical solution, i.e. $V_0 =$ constant ($>0$) and $H_0 = fV_0^2/8\sin\theta$, even for Froude numbers much larger than 2 (e.g. $Fr_p = 10$). In that scenario the background flow is also unstable [1, 3] but we do not observe the development of instability about the steady flow with moving water.

## 4 Summary and Conclusions

In this article we have computed the evolution of small disturbances (16) about a background flow which is essentially a kinematic wave [1] by using several well-balanced finite volume methods [8, 9]. Independent of the spatial order of accuracy, we have shown that all the numerical techniques are able to simulate with success the attenuation of infinitesimal disturbances for a $Fr_p$ value (7) equal to 2, although first- and second-order methods fail to reproduce the correct phase speed. In addition, the authors have also verified that the numerical schemes are able to reproduce a unstable, steady, uniform flow (i.e. $\phi = 0$) over a constant slope with $Fr_p > 2$. On the other hand, for $Fr_p = 4 > Fr_{cr}(\phi)$ (8) and $\phi = O(10^{-4})$ (9), the numerical simulations corresponding to stable disturbances with $\lambda = \lambda_0 = 1$ exhibit the development of free-surface instabilities. The origin of the hydrodynamic instabilities is attributed to the development of wave packets with typical wavelengths of $\lambda = 8\Delta X$, see Fig. 6, which are much shorter than those of the simulated disturbances ($\lambda = 1$) and have positive physical growth rates, as shown in Fig. 7. Because these numerical instabilities appear in the simulation of both the background and of the perturbed flow, the origin of the problem might be the stiff source term which fixes the value of $Fr_p$ (7). Therefore, this benchmark may serve to check more sophisticated and accurate techniques valid for out-equilibrium shallow-water flows [4, 5] with stiff source terms [6] and, in particular, to check the performance of low dissipative high-order well-balanced filter schemes for non-equilibrium flows [7] with variable cut-off wavenumber [13].

We conclude by pointing out that the present work, as well as [3], could be extended by the inclusion of a further term in the momentum balance equation (4) that accounts for

energy dissipation by shearing normal to the flow, as Needham and Merkin [10] did with Dressler's solution. So unrealistic extreme short wavelengths could be attenuated.

**Acknowledgements** The computer time was provided by the Centro de Supercomputación de Galicia (CESGA) under project number ICTS-CESGA 142.

## References

1. Lighthill, M., Whitham, G.: On kinematic waves. Part I. Flood movement in long rivers. Part II. Theory of traffic flow on long crowded roads. Proc. R. Soc. A (London) **229**, 281–345 (1955)
2. Brock, R.R.: Development of roll-wave trains in open channels. J. Hydraul. Div. **95**, 1401–1427 (1969)
3. Bohorquez, P.: Competition between kinematic and dynamic waves in floods on steep slopes. J. Fluid Mech. **645**, 375–409 (2010)
4. Castro, M., Gallardo, J.M., Parés, C.: High order finite volume schemes based on reconstruction of states for solving hyperbolic systems with nonconservative products. Applications to shallow-water systems. Math. Comput. **75**, 1103–1134 (2006)
5. Noelle, S., Xing, Y., Shu, C.-W.: High-order well-balanced finite volume WENO schemes for shallow water equation with moving water. J. Comput. Phys. **226**, 29–58 (2007)
6. Dumbser, M., Enaux, C., Toro, E.F.: Finite volume schemes of very high order of accuracy for stiff hyperbolic balance laws. J. Comput. Phys. **227**, 3971–4001 (2008)
7. Wang, W., Yee, H.C., Sjögreen, B., Magin, T., Shu, C.-W.: Construction of low dissipative high-order well-balanced filter schemes for non-equilibrium flows. J. Comput. Phys. doi:10.1016/j.jcp.2010.04.033
8. Burguete, J., García-Navarro, P.: Efficient construction of high-resolution TVD conservative schemes for equations with source terms: application to shallow water flows. Int. J. Numer. Methods Fluids **37**(2), 209–248 (2001)
9. Črnjarić Žic, N., Vuković, S., Sopta, L.: Balanced finite volume WENO and central WENO schemes for the shallow water and the open-channel flow equations. J. Comput. Phys. **200**, 512–548 (2004)
10. Needham, D.J., Merkin, J.H.: On roll waves down an open inclined channel. Proc. R. Soc. A (London) **394**, 259–278 (1984)
11. Gottlieb, S., Ketcheson, D.I., Shu, C.-W.: High order strong stability preserving time discretizations. J. Sci. Comput. **38**(3), 251–289 (2009)
12. Ketcheson, D.I., LeVeque, R.J.: WENOCLAW: a higher order wave propagation method. In: Benzoni-Gavage, S., Serre, D. (eds.) Hyperbolic Problems: Theory, Numerics, Applications, pp. 609–616. Springer, Berlin (2008)
13. Kim, J.W.: High-order compact filters with variable cut-off wavenumber and stable boundary treatment. Comput. Fluids **39**, 1168–1182 (2010)